In-situ growth of CdS quantum dots on g-C3N4 nanosheets for highly efficient photocatalytic hydrogen generation under visible light irradiation

Cao, Shao-Wen; Yuan, Yu-Peng; Fang, Jun; Mohammad Mehdi Shahjamali; Barber, James; Boey, Freddy Yin Chiang; Loo, Say Chye Joachim; Xue, Can

2012

Cao, S., Yuan, Y., Fang, J., Mohammad, M. S., Boey, F. Y. C., Barber, J., et al. (2012). In-situ growth of CdS quantum dots on g-C3N4 nanosheets for highly efficient photocatalytic hydrogen generation under visible light irradiation. International Journal of Hydrogen Energy, 38(3), 1258-1266.

https://hdl.handle.net/10356/96940

https://doi.org/10.1016/j.ijhydene.2012.10.116

In-situ Growth of CdS Quantum Dots on g-C_3N_4 Nanosheets for Highly Efficient Photocatalytic Hydrogen Generation under Visible Light Irradiation

Shao-Wen Cao [a], Yu-Peng Yuan [a,b], Jun Fang [a], Mohammad Mehdi Shahjamali[a], Freddy Y. C. Boey [a], James Barber [a,c], Say Chye Joachim Loo [a,]*, Can Xue[a,]*

[a]*Solar Fuels Lab, School of Materials Science and Engineering, Nanyang Technological University, 50 Nanyang Avenue, Singapore 639798 (Singapore)*

[b]*Laboratory of Advanced Porous Materials, School of Chemistry and Chemical Engineering, An hui University, Hefei, 230039, P.R.China*

[c]*Division of Molecular Biosciences, Imperial College London, South Kensington Campus London SW7 2AZ, U.K.*

*Corresponding author. E-mail: cxue@ntu.edu.sg; joachimloo@ntu.edu.sg.

Absrtract

Well dispersed CdS quantum dots were successfully grown in-situ on g-C_3N_4 nanosheets through a solvothermal method involving dimethyl sulfoxide. The resultant CdS-C_3N_4 nanocomposites exhibit remarkably higher efficiency for photocatalytic hydrogen evolution under visible light irradiation as compared to pure g-C_3N_4. The optimal composite with 12 wt% CdS showed a hydrogen evolution rate of 4.494 $mmol \cdot h^{-1} \cdot g^{-1}$, which is more than 115 times higher than that of pure g-C_3N_4. The enhanced photocatalytic activity induced by the in-situ grown CdS quantum dots is attributed to the interfacial transfer of photogenerated electrons and holes between g-C_3N_4 and CdS, which leads to effective charge separation on both parts.

Keywords: Solar fuels; Hydrogen production; Water splitting; carbon nitride; Photocatalyst; Charge transfer.

1. Introduction

Efficient conversion of solar energy into hydrogen fuels through photocatalytic water splitting is of great importance for the future of sustainable energy. Since the first discovery of hydrogen production by photocatalytic water splitting over Pt/TiO_2 in 1972 [1], great efforts have been made by researchers for photocatalytic generation of hydrogen from water. To date, many semiconductors, such as TiO_2 [2-4], Cu_2O [5,6], $SrTiO_3$ [7,8], $ZnFe_2O_4$ [9], CdS [10,11], $InVO_4$ [12,13] etc., have been reported as photocatalysts for hydrogen generation. Recently, graphitic carbon nitride ($g\text{-}C_3N_4$) has been introduced as a promising visible light photocatalyst for water reduction and oxidation due to its unique electronic band structure and high stability [14,15]. To advance this promising photocatalytic material, researchers have coupled $g\text{-}C_3N_4$ with various semiconductors, such as TiO_2 [16], ZnO [17,18], TaON [19], $ZnWO_4$ [20], $BiPO_4$ [21] and Bi_2WO_6 [22], to increase the separation efficiency of photogenerated electron-hole pairs, thus to promote the photocatalytic activity.

As a well-known II–VI semiconductor, CdS nanocrystals are attractive photocatalytic materials for solar-to-fuels conversion because its band gap (2.4 eV) allows for efficient visible light absorption, and the reduction and oxidation potentials of water lie within the band edges of CdS [23]. However, several drawbacks still limit the photocatalytic efficiency on pure CdS nanoparticles. For example, the CdS nanocrystals tend to aggregate into larger particles, leading to reduced surface area and higher charge recombination rates [24]. Therefore, improvement of the performance of CdS naoparticles has been numerously studied on the composites combining CdS with other components, including noble metals [25,26], graphene [27,28], graphene oxide [29,30], TiO_2 [31,32], ZnO [33,34], CdSe [35], ZnS [36,37], and so on. Wu et al. have found that one- and two-dimensional nanostructures offer higher charge mobility and lower recombination

rates of charge carriers than zero-dimensional nanoparticles [38,39]. Hence, implanting 2-D semiconductor nanostructures into composite photocatalysts may also improve the photocatalytic activity. Very recently, Feng et al. prepared CdS/g-C_3N_4 composites by the chemical impregnation and subsequent calcination of the separately prepared CdS particles and g-C_3N_4 [40]. The CdS/g-C_3N_4 composites with 30 wt% CdS showed ~9 times higher hydrogen evolution rate than the pure g-C_3N_4. Nevertheless, the calcinations process still caused severe aggregation of CdS nanoparticles, which restricted the utilization of photocatalytic function of CdS.

Herein, we present the in-situ growth of CdS quantum dots (QDs) on g-C_3N_4 nanosheets through a dimethyl sulfoxide (DMSO) involved solvothermal method, and employ the obtained CdS/g-C_3N_4 composites for visible-light-driven photocatalytic hydrogen evolution. The characterization results revealed that CdS QDs are well dispersed on the surface of the g-C_3N_4 nanosheets, and the aggregation of CdS QDs is successfully inhibited during both the solvothermal process and the photocatalytic test. At an optimal CdS content of 12 wt%, the CdS/g-C_3N_4 nanocomposite exhibits more than 115 times higher hydrogen evolution rate than the pure g-C_3N_4. These results demonstrate that our CdS/g-C_3N_4 nanocomposites are highly efficient photocatalysts for hydrogen generation under visible light irradiation.

2. Experimental

2.1 Preparation of CdS-C_3N_4 nanocomposites

The g-C_3N_4 nanosheets were synthesized according to a literature method [41]. Melamine powder (6 g) was heated in an alumina crucible with a cover in a muffle furnace at 500 ºC for 2 h, and further heated to 520 ºC for another 2 h to generate g-C_3N_4 nanosheets. In-situ growth of CdS QDs (12 wt%) on g-C_3N_4 nanosheets was carried out by adding 133 mg of $Cd(Ac)_2 \cdot 2H_2O$

and 500 mg of the as-prepared g-C_3N_4 into 50 mL DMSO with stirring. The obtained suspension was transferred into a 100-mL teflon-lined stainless-steel autoclave, and then was heated to 180 ºC and kept at this temperature for 12 h. After natural cooling to room temperature, the product was collected and washed using centrifugation-redispersion cycles with water and ethanol repeatedly. After that, the as-obtained powder was dried in a vacuum oven. Pure CdS, and CdS-C_3N_4 nanocomposites with other CdS loading amount were synthesized using the similar route by adjusting the dosage of g-C_3N_4.

2.2 Characterization

A Shimadzu XRD-6000 X-ray diffractometer (Cu Kα source) was used to record X-ray powder diffraction (XRD) patterns with the 2θ range from 5 to 80° at a scan rate of 1 °/min. Energy dispersive X-ray (EDX) spectra and transmission electron microscopy (TEM) images were obtained from a JEOL JEM-2100F transmission electron microscope at an accelerating voltage of 200 kV. A JEOL JSM-7600F scanning electron microscope was used to acquire scanning electron microscopy (SEM) images. UV–vis diffuse reflectance spectra (DRS) were taken with a Lambda 750 UV/Vis/NIR spectrophotometer (Perkin Elmer, USA). X-ray Photoelectron spectroscopy (XPS) measurement was performed on a Thermo Scientific Theta Probe XPS with monochromatized Al Kα (*hv*=1486.6 eV) source. The BET surface areas were measured on a Micromeritics ASAP 2020M$^+$C system. The photoluminescence (PL) spectra were obtained by a Shimazu RF-5310PC fluorometer at an excitation wavelength of 325 nm.

2.3 Photocatalytic hydrogen evolution from water reduction

In a typical experiment, 5 mg of the prepared photocatalysts were dispersed in 10 mL aqueous solution of 0.1 M L-ascorbic acid. The pH value was adjusted to 4.0 with 1 M NaOH aqueous solution. 0.5 wt% Pt co-catalyst was loaded by adding 60.7 µL of H_2PtCl_6 (0.08 wt%) aqueous

solution into the suspension followed by the irradiation of a 300-W xenon lamp (MAX-302, Asahi Spectra, USA) coupled with a UV cut-off filter (λ > 420 nm). Before sealed in a quartz flask, the suspension was purged with nitrogen for 3 h to drive away the residual air The photocatalytic hydrogen production was then performed by irradiating the suspension with a 300-W xenon lamp (MAX-302, Asahi Spectra, USA) coupled with a UV cut-off filter (λ > 420 nm). The gas product composition was analyzed every 60 min through an Agilent 7890A gas chromatograph (GC) with TCD detector. The apparent quantum efficiency (QE) was estimated by using the following equation.

$$QE = \frac{2\times \ the \ \ number \ \ of \ \ evolved \ \ hydrogen \ \ molecules}{the \ \ number \ \ of \ \ incident \ \ photons} \times 100\%$$

3. Results and discussion

The XRD patterns of the as-prepared pure g-C_3N_4, pure CdS, and CdS-C_3N_4 nanocomposites with 12 wt% CdS are shown in Fig. 1. Two pronounced diffraction peaks are found at 27.4º and 13.1º for pure g-C_3N_4, corresponding to the characteristic interlayer stacking peak of aromatic systems (indexed for graphitic materials as the 002 peak), and the interplanar separation (indexed as the 100 peak), respectively, which is consistent with the XRD pattern reported in the literature [41]. The XRD pattern of pure CdS gives rise to four distinct diffraction peaks at 26.7º, 44.1º, 52.2º, and 70.5º, which can be attributed to the (111), (220), (311), and (331) crystal planes of hawleyite CdS (JCPDS No. 75-0581), respectively. The XRD pattern of CdS-C_3N_4 nanocomposites shows diffraction peaks of both CdS and g-C_3N_4, while the characteristic peaks of CdS (26.7º) and g-C_3N_4 (27.4º) were very close and overlap with each other.

SEM and TEM images were taken to directly analyze the structures of the samples and particularly the effect of g-C_3N_4 on the morphology of CdS QDs, as displayed in Fig. 2. It can be observed from Fig 2a-c that pure g-C_3N_4 shows a nanosheet structure with smooth surfaces. Fig. 2d and 2e indicate significant aggregation of the CdS nanoparticles into spheres with more than 100 nm diameter in the pure CdS sample. However, surprisingly, when the g-C_3N_4 nanosheets were present during the solvothermal process, we observed very small CdS QDs spreading on the g-C_3N_4 nanosheets (Fig. 2f and 2g), and no free CdS nanoparticles were present in the suspension. The HRTEM image (Fig. 2h) shows that the average size of CdS QDs is around 5 nm. The lattice fringes with d-spacing of 0.336 nm can be assigned to the (111) crystal plane of hawleyite CdS. These results indicate that the g-C_3N_4 nanosheets significantly influence the growth process of CdS nanoparticles and effectively restrain their aggregations. This could be attributed to two major reasons. First, the g-C_3N_4 nanosheet may act as a two-dimensional "mat" that interacts with CdS QDs through physisorption to hinder their aggregation. Second, the oxygen-containing defects and the amino groups on g-C_3N_4 surfaces could serve as anchor sites to immobilize Cd precursors as well as CdS QDs on the g-C_3N_4 nanosheet, which prevents the aggregation of CdS QDs from surface diffusion on g-C_3N_4.

The optical properties of pure g-C_3N_4, pure CdS, and CdS-C_3N_4 nanocomposites were revealed by UV-vis diffuse reflectance spectroscopy (DRS). As shown in Fig. 3, the pure g-C_3N_4 exhibits an absorption edge at 451 nm, corresponding to the band gap of 2.75 eV. The pure CdS sample has an absorption edge at 514 nm, which can be attributed to the CdS band gap of 2.41 eV. The CdS-C_3N_4 nanocomposite (with 12 wt% CdS) shows hybrid absorption features of g-C_3N_4 and CdS, which allows for more efficient utilization of the solar spectrum to create photogenerated electrons and holes.

The CdS-C_3N_4 sample (with 12 wt% CdS) was further investigated by XPS measurements. As shown in Fig. 4, the C 1s spectrum can be deconvoluted into three peaks at 284.8 eV, 286.2 eV and 288.2 eV. The former peak is typically ascribed to sp^2 C–C bonds, and the last (288.2 eV) is identified as sp^2-bonded carbon in N-containing aromatic rings (N–C=N), which represent the major carbon species in the g-C_3N_4 [42,43]. The weak feature at 286.2 eV could be assigned to sp^3-coordinated carbon bonds from the defects on g-C_3N_4 surfaces [15]. The corresponding binding energies of N 1s spectrum are determined to be 398.7 eV, 400.0 eV, and 401.1 eV. The main peak centered at 398.7 eV originates from the sp^2-bonded N involved in the triazine rings (C–N=C) dominated in g-C_3N_4. While the weak peak at 400.0 eV is caused by the tertiary nitrogen N–$(C)_3$ groups, and another weak peak at 401.1 eV indicates the presence of amino groups (C–N–H) [44,45]. The photoelectron peaks for Cd 3d were observed at 404.9 and 411.7 eV (Fig. 4c), which can be assigned to the Cd^{2+} ions of the CdS QDs [46]. Fig. 4d shows the S 2p peak at 161.2 and 162.4 eV, as expected for the sulfide in CdS QDs [47].

Photocatalytic hydrogen evolution activity of the prepared CdS-C_3N_4 nanocomposites was evaluated under visible light ($\lambda > 420$ nm) irradiation by using L-ascorbic acid as the sacrificial reagent to quench photoinduced holes, and 0.5 wt% Pt was added as co-catalyst to reduce the overpotential for hydrogen evolution. Fig. 5 summarizes the H_2 evolution rate by pure g-C_3N_4, pure CdS, and CdS-C_3N_4 nanocomposites with various CdS ratio. In-situ growth of CdS QDs on g-C_3N_4 nanosheets noticeably improves the photocatalytic hydrogen evolution activity. Even with only 3 wt% CdS QDs, the CdS-C_3N_4 composite exhibit a hydrogen evolution rate of 2.333 $mmol \cdot h^{-1} \cdot g^{-1}$, which is more than 60 times higher than that of pure g-C_3N_4 (0.038 $mmol \cdot h^{-1} \cdot g^{-1}$). The highest photocatalytic activity was achieved at 12 wt% CdS with a hydrogen evolution rate

of 4.494 $mmol \cdot h^{-1} \cdot g^{-1}$, and the apparent quantum efficiency is estimated as 8.0 % at 420 nm. It is even far beyond the performance of pure CdS (2.486 $mmol \cdot h^{-1} \cdot g^{-1}$).

Actually, if normalized with the mass concentration of CdS, the hydrogen evolution rate would show more remarkable disparity between 12 wt% CdS-C_3N_4 (37.450 $mmol \cdot h^{-1} \cdot g^{-1}$) and pure CdS (2.486 $mmol \cdot h^{-1} \cdot g^{-1}$). We have also measured the BET surface areas of pure CdS (22.1 $m^2 \cdot g^{-1}$), pure g-C_3N_4 nanosheets (5.4 $m^2 \cdot g^{-1}$), and 12 wt% CdS-C_3N_4 (9.5 $m^2 \cdot g^{-1}$). Although 12 wt% CdS-C_3N_4 has lower surface area, it still exhibits much higher photocatalytic activity than pure CdS. If normalized with the surface areas of the samples, the hydrogen evolution rates would be 0.112 $mmol \cdot h^{-1} \cdot m^{-2}$, 0.007 $mmol \cdot h^{-1} \cdot m^{-2}$, and 0.473 $mmol \cdot h^{-1} \cdot m^{-2}$ for pure CdS, pure g-C_3N_4 nanosheets, and 12 wt% CdS-C_3N_4, respectively. This indicates that the surface area is not crucial to the photocatalytic activities of CdS-C_3N_4 composites.

The enhanced photocatalytic activities of CdS-C_3N_4 composite are attributed to the synergic effect between C_3N_4 and CdS, which plays a key role to the effective separation of photogenerated electron-hole pairs and the photocatalytic reactive sites. At lower CdS content, a good dispersion of CdS QDs on the g-C_3N_4 surface could be achieved. In this case, the increase of CdS content would lead to more CdS QDs generated on the g-C_3N_4 surface, which creates larger CdS-C_3N_4 interface area and allows more efficient charge transfer between g-C_3N_4 and CdS QDs. However, excess CdS loading causes considerable aggregation of CdS QDs. As shown in Fig. 6, for the composite sample with 18 wt% CdS, a portion of CdS QDs aggregated into big spheres adhering on the g-C_3N_4 surface. Such aggregations reduce the interface area between CdS and g-C_3N_4, thereby decrease the charge separation efficiency relying on interfacial charge transfer. Therefore, there is a balance between CdS loading amount and CdS-C_3N_4

interface area. And our studies revealed an optimal loading of 12 wt% CdS on g-C_3N_4, which showed the best photocatalytic activity.

In addition, the optimal 12 wt% CdS-C_3N_4 composite exhibits fairly stable photocatalytic activity. Fig. 7a shows that the hydrogen evolution rate remains consistent even at the prolonged time period of 24 h. The recycling capability of the 12 wt% CdS-C_3N_4 was verified by carrying out a four-run test of photocatalytic hydrogen evolution. Fig. 7b reveals that no obvious decrease of H_2 evolution was observed after the four-run test. Fig 8 shows the re-characterization results of the 12 wt% CdS-C_3N_4 sample after being used for cycling photocatalytic experiments. The XRD pattern remains no change comparing to that of the freshly prepared 12 wt% CdS-C_3N_4 sample (Fig. 1), suggesting the crystal structures of the composite were not altered during the photocatalytic tests. The TEM image (Fig. 8b) indicates that the CdS QDs were still well dispersed on the g-C_3N_4 nanosheets after cycling photocatalytic experiments. Although it is difficult to identify the crystal lattice of CdS in the high-magnification TEM image (Fig. 8c) due to the photodeposition of Pt on the composite sample, the corresponding EDX spectrum (Fig. 8d) from the area of Fig. 8c indicates the co-existence of CdS and Pt with an atomic ratio of around 18:1. While on the other surface area of g-C_3N_4 nanosheets without CdS nanoparticles, Pt was hardly observed in EDX analysis. This observation suggests that Pt may be only grown onto the CdS QDs upon photoexcitation of the CdS-C_3N_4 composite. It also implies the photoinduced electron transfer from g-C_3N_4 to CdS, rather than the reversed way.

On the basis of the above experimental results, we believe that the enhanced photocatalytic activity induced by the in-situ grown CdS QDs is attributed to the interfacial transfer of photogenerated electrons and holes between g-C_3N_4 and CdS, which leads to effective charge separation on both parts. This assumption is supported by photoluminescence (PL)

measurements. Fig. 9 shows that at an excitation wavelength of 325 nm, the pure g-C_3N_4 sample exhibits a strong emission peak centered at ~450 nm. In comparison, this intensity of this emission band drops significantly when for the composite sample with 12 wt% CdS. This indicates an efficient transfer of photoexcited electrons from g-C_3N_4 to CdS QDs.

Fig. 10 shows the schematic illustration of the possible photocatalytic mechanism. Both CdS and g-C_3N_4 can absorb visible light to produce photoinduced electron-hole pairs. Since the conduction band (CB) position of CdS (~ -0.5 eV vs. NHE [48]) is lower than that of g-C_3N_4 (~ -1.1 eV vs. NHE [19]), the photoinduced electrons on the CB of g-C_3N_4 can directly transfer to the CB of CdS. These electrons, together with the electrons excited from the VB of CdS, will accumulate on the Pt deposited on CdS nanoparticle surfaces. While the corresponding valence band (VB) position of CdS (~ +1.9 eV vs. NHE) is lower than that of g-C_3N_4 (~ +1.6 eV vs. NHE), the photogenerated holes on the VB of CdS can immigrate to the VB of g-C_3N_4. Therefore, an effective charge separation can be achieved, resulting in longer lifetime of the photogenerated electrons and holes for enhanced photocatalytic activity. As a result, the photoinduced holes can oxidize L-ascorbic acid (H_2A) on the g-C_3N_4 surface, and meanwhile the separated electrons will have longer time to reduce H^+ to H_2 on the Pt nanoparticle surface.

4. Conclusions

In summary, well dispersed CdS QDs have been successfully grown in-situ on g-C_3N_4 nanosheets through a DMSO involved solvothermal method. The resulting CdS-C_3N_4 nanocomposites exhibit high efficiency of hydrogen evolution from photocatalytic water reduction under visible light irradiation due to the efficient charge separation through the interfaces between CdS QDs and g-C_3N_4 nanosheets. The optimal composite with 12 wt% CdS showed a hydrogen evolution rate of 4.494 $mmol \cdot h^{-1} \cdot g^{-1}$, which is more than 115 times higher

than that of pure g-C_3N_4. This work not only introduces a simple strategy to in-situ grow metal sulfide nanoparticles on carbon nitride surfaces, but also demonstrates that the g-C_3N_4-based nanomaterials can serve as highly efficient photocatalysts for solar hydrogen generation when effective charge separation is achieved.

Acknowledgement

This work is financially supported by NTU Start-Up Grant (SUG), NTU seed funding for Solar Fuels Laboratory, MOE AcRF-Tier1 RG 44/11, and CRP (NRF-CRP5-2009-04) from NRF Singapore. Y. P. Yuan acknowledges the support from the National Natural Science Foundation of China (No. 51002001).

References

[1] Fujishima A, Honda K. Electrochemical photolysis of water at a semiconductor electrode. Nature 1972;238:37-8.

[2] Antony RP, Mathews T, Ramesh C, Murugesan N, Dasgupta A, Dhara S, et al. Efficient photocatalytic hydrogen generation by Pt modified TiO_2 nanotubes fabricated by rapid breakdown anodization. Int J Hydrogen Energy 2012;37:8268-76.

[3] Babu VJ, Kumar MK, Nair AS, Kheng TL, Allakhverdiev SI, Ramakrishna S. Visible light photocatalytic water splitting for hydrogen production from N-TiO_2 rice grain shaped electrospun nanostructures. Int J Hydrogen Energy 2012;37:8897-904.

[4] Xu H, Chen XQ, Ouyang SX, Kako T, Ye JH. Size-dependent mie's scattering effect on TiO_2 spheres for the superior photoactivity of H_2 evolution. J Phys Chem C 2012;116:3833-9.

[5] Somasundaram S, Chenthamarakshan CRN, De tacconi NR, Rajeshwar K. Photocatalytic production of hydrogen from electrodeposited p-Cu_2O film and sacrificial electron donors. Int J Hydrogen Energy 2007;32:4661-9.

[6] Tran PD, Batabyal SK, Pramana SS, Barber J, Wong LH, Loo SC. A cuprous oxide-reduced graphene oxide (Cu_2O-rGO) composite photocatalyst for hydrogen generation: employing rGO as an electron acceptor to enhance the photocatalytic activity and stability of Cu_2O. Nanoscale 2012;4:3875-8.

[7] Liu J, Sun Y, Li Z, Li S, Zhao J. Photocatalytic hydrogen production from water/methanol solutions over highly ordered Ag–$SrTiO_3$ nanotube arrays. Int J Hydrogen Energy 2011;36:5811-6.

[8] Ouyang SX, Tong H, Umezawa N, Cao JY, Li P, Bi YP, et al. Surface-alkalinization-induced enhancement of photocatalytic H_2 evolution over $SrTiO_3$-based photocatalysts. J Am Chem Soc 2012;134:1974−7.

[9] Lv H, Ma L, Zeng P, Ke D, Peng T. Synthesis of floriated $ZnFe_2O_4$ with porous nanorod structures and its photocatalytic hydrogen production under visible light. J Mater Chem 2010;20:3665.

[10] He K, Li M, Guo L. Preparation and photocatalytic activity of PANI-CdS composites for hydrogen evolution. Int J Hydrogen Energy 2012;37:755-9.

[11] Girginer B, Galli G, Chiellini E, Bicak N. Preparation of stable CdS nanoparticles in aqueous medium and their hydrogen generation efficiencies in photolysis of water. Int J Hydrogen Energy 2009;34:1176-84.

[12] Cao SW, Fang J, Shahjamali MM, Boey FYC, Barber J, Loo SCJ, Xue C. Plasmon-Enhanced Hydrogen Evolution on Au-$InVO_4$ Hybrid Microspheres. RSC Adv 2012;2:5513-15.

[13] Cao SW, Yin Z, Barber J, Boey FYC, Loo SCJ, Xue C. Preparation of Au-$BiVO_4$ Heterogeneous Nanostructures as Highly Efficient Visible-Light Photocatalysts, ACS Appl Mater Interfaces 2012; 4; 418-23.

[14] Wang XC, Maeda K, Thomas A, Takanabe K, Xin G, Carlsson JM, et al. A metal-free polymeric photocatalyst for hydrogen production from water under visible light. Nat Mater 2009;8:76-80.

[15] Zhang G, Zhang J, Zhang M, Wang X. Polycondensation of thiourea into carbon nitride semiconductors as visible light photocatalysts. J Mater Chem 2012;22:8083.

[16] Yan H, Yang H. TiO_2–g-C_3N_4 composite materials for photocatalytic H_2 evolution under visible light irradiation. J Alloy Compd 2011;509:L26-L9.

[17] Wang Y, Shi R, Lin J, Zhu Y. Enhancement of photocurrent and photocatalytic activity of ZnO hybridized with graphite-like C_3N_4. Energy Environ Sci 2011;4:2922.

[18] Sun JX, Yuan YP, Qiu LG, Jiang X, Xie AJ, Shen YH, et al. Fabrication of composite photocatalyst g-C_3N_4-ZnO and enhancement of photocatalytic activity under visible light. Dalton Trans 2012;41:6756-63.

[19] Yan SC, Lv SB, Li ZS, Zou ZG. Organic-inorganic composite photocatalyst of g-C_3N_4 and TaON with improved visible light photocatalytic activities. Dalton Trans 2010;39:1488-91.

[20] Wang Y, Wang Z, Muhammad S, He J. Graphite-like C3N4 hybridized $ZnWO_4$ nanorods: Synthesis and its enhanced photocatalysis in visible light. Crystengcomm 2012;14:5065.

[21] Pan C, Xu J, Wang Y, Li D, Zhu Y. Dramatic Activity of C_3N_4/$BiPO_4$ Photocatalyst with core/shell structure formed by self-assembly. Adv Funct Mater 2012;22:1518-24.

[22] Ge L, Han C, Liu J. Novel visible light-induced g-C_3N_4/Bi_2WO_6 composite photocatalysts for efficient degradation of methyl orange. Appl Catals B Environ 2011;108-109:100-7.

[23] Jing DW, LJ G. A novel method for the preparation of a highly stable and active CdS photocatalyst with a special surface nanostructure. J Phys Chem B 2006;110:11139-45.

[24] Li Q, Guo B, Yu J, Ran J, Zhang B, Yan H, et al. Highly efficient visible-light-driven photocatalytic hydrogen production of CdS-cluster-decorated graphene nanosheets. J Am Chem Soc 2011;133:10878-84.

[25] Chen WT, Yang TT, YJ H. Au-CdS core-shell nanocrystals with controllable shell thickness and photoinduced charge separation property. Chem Mater 2008:7204–6.

[26] Sheeney-Haj-Ichia L, Pogorelova S, Gofer Y, Willner I. Enhanced photoelectrochemistry in CdS/Au nanoparticle bilayers. Adv Funct Mater 2004;14:416-24.

[27] Zhang N, Zhang Y, Pan X, Fu X, Liu S, Xu Y-J. Assembly of CdS nanoparticles on the two-dimensional graphene scaffold as visible-light-driven photocatalyst for selective organic transformation under ambient conditions. J Phys Chem C 2011;115:23501-11.

[28] Jia L, Wang D-H, Huang Y-X, Xu A-W, Yu H-Q. Highly durable N-doped graphene/CdS nanocomposites with enhanced photocatalytic hydrogen evolution from water under visible light irradiation. J Phys Chem C 2011;115:11466-73.

[29] Gao P, Liu J, Lee S, Zhang T, Sun DD. High quality graphene oxide–CdS–Pt nanocomposites for efficient photocatalytic hydrogen evolution. J Mater Chem 2012;22:2292.

[30] Liu X, Pan L, Lv T, Zhu G, Sun Z, Sun C. Microwave-assisted synthesis of CdS-reduced graphene oxide composites for photocatalytic reduction of Cr(VI). Chem Commun 2011;47:11984-6.

[31] Luo J, Ma L, He T, Ng CF, Wang S, Sun H, et al. TiO_2/(CdS, CdSe, CdSeS) nanorod heterostructures and photoelectrochemical properties. J Phys Chem C 2012;116:11956-63.

[32] Qian S, Wang C, Liu W, Zhu Y, Yao W, Lu X. An enhanced CdS/TiO_2 photocatalyst with high stability and activity: Effect of mesoporous substrate and bifunctional linking molecule. J Mater Chem 2011;21:4945.

[33] Xu F, Yuan Y, Han H, Wu D, Gao Z, Jiang K. Synthesis of ZnO/CdS hierarchical heterostructure with enhanced photocatalytic efficiency under nature sunlight. Crystengcomm 2012;14:3615.

[34] Wang X, Yin L, Liu G, Wang L, Saito R, Lu GQ, et al. Polar interface-induced improvement in high photocatalytic hydrogen evolution over ZnO–CdS heterostructures. Energy Environ Sci 2011;4:3976.

[35] Thibert A, Frame FA, Busby E, Holmes MA, Osterloh FE, Larsen DS. Sequestering high-energy electrons to facilitate photocatalytic hydrogen generation in CdSe/CdS nanocrystals. J Phys Chem Lett 2011;2:2688-94.

[36] Zhang K, Jing D, Chen Q, Guo L. Influence of Sr-doping on the photocatalytic activities of CdS–ZnS solid solution photocatalysts. Int J Hydrogen Energy 2010;35:2048-57.

[37] Wang L, Wei H, Fan Y, Liu X, Zhan J. Synthesis, optical properties, and photocatalytic activity of one-dimensional CdS@ZnS core-shell nanocomposites. Nanoscale Res Lett 2009;4:558-64.

[38] Wu NQ, Wang J, Tafen DN, Wang H, Zheng J-G, Lewis JP, et al. Shape-enhanced photocatalytic activity of single-crystalline anatase TiO_2 (101) nanobelts. J Am Chem Soc 2010;132:6679-85.

[39] Meng FK, Hong ZL, Arndt J, Li M, Zhi MJ, Yang F, et al. Visible light photocatalytic activity of nitrogen-doped $La_2Ti_2O_7$ nanosheets originating from band gap narrowing. Nano Res 2012;5:213–21.

[40] Ge L, Zuo F, Liu J, Ma Q, Wang C, Sun D, Bartels L, Feng PY. Synthesis and efficient visible light photocatalytic hydrogen evolution of polymeric g-C_3N_4 coupled with CdS quantum dots. J Phys Chem C 2012;116:13708-14.

[41] Yan SC, Li ZS, Zou ZG. Photodegradation performance of g-C_3N_4 fabricated by directly heating melamine. Langmuir 2009;25:10397-401.

[42] Wang Y, Wang X, Antonietti M. Polymeric graphitic carbon nitride as a heterogeneous organocatalyst: from photochemistry to multipurpose catalysis to sustainable chemistry. Angew Chem Int Ed 2012;51:68-89.

[43] Vinu A. Two-dimensional hexagonally-ordered mesoporous carbon nitrides with tunable pore diameter, surface area and nitrogen content. Adv Funct Mater 2008;18:816-27.

[44] Thomas A, Fischer A, Goettmann F, Antonietti M, Müller J-O, Schlögl R, et al. Graphitic carbon nitride materials: variation of structure and morphology and their use as metal-free catalysts. J Mater Chem 2008;18:4893.

[45] Xiang Q, Yu J, Jaroniec M. Preparation and enhanced visible-light photocatalytic H_2-production activity of graphene/C_3N_4 Composites. J Phys Chem C 2011;115:7355-63.

[46] Chu J, Li X, Qi J. Hydrothermal synthesis of CdS microparticles–graphene hybrid and its optical properties. Crystengcomm 2012;14:1881.

[47] Colvin VL, Goldstein AN, Alivisatos AP. Semiconductor nanocrystals covalently bound to metal surfaces with self-assembled monolayers. J Am Chem Soc 1992;114:5221-30.

[48] Sobczynski A, Bard AJ, Campion A, Fox MA, Mallouk T, Webber SE, et al. Photoassisted hydrogen generation: Pt and CdS supported on separate particles. J Phys Chem 1987;91:3316-20.

Figure Legends

Fig. 1 XRD patterns of pure g-C_3N_4, pure CdS, and 12 wt% CdS-C_3N_4.

Fig. 2 (a) SEM and (b,c) TEM images of pure g-C_3N_4; (d) SEM and (e) TEM images of pure CdS; (f) SEM and (g,h) TEM images of 12 wt% CdS-C_3N_4.

Fig. 3 Absorption spectra (converted from UV–vis diffuse reflectance spectra) of pure g-C_3N_4, pure CdS, and 12 wt% CdS-C_3N_4.

Fig. 4 XPS spectra for 12 wt% CdS-C_3N_4: (a) C 1s; (b) N 1s; (c) Cd 3d; (d) S 2p.

Fig. 5 (a) Comparison of the visible light induced H_2 evolution rate for different samples; (b) Plots of photocatalytic H_2 evolution amount versus irradiation ($\lambda > 420$ nm) time for different samples.

Fig. 6 TEM image of 18 wt% CdS-C_3N_4.

Fig. 7 (a) Photocatalytic H_2 evolution curve with prolonged irradiation time for 12 wt% CdS-C_3N_4; (b) Cycling test of photocatalytic H_2 evolution for 12 wt% CdS-C_3N_4.

Fig. 8 Characterization of 12 wt% CdS-C_3N_4 after being used in cycling photocatalytic tests: (a) XRD pattern; (b,c) TEM images; (d) EDX spectrum taken from the area of image (c).

Fig. 9 Photoluminescence spectra for pure g-C_3N_4 and the 12 wt% CdS-C_3N_4 at an excitation wavelength of 325 nm.

Fig. 10 Schematic illustration of visible light induced photocatalytic process for H_2 evolution on the CdS-C_3N_4 nanocomposites, in which H_2A and HA• refers to ascorbic acid and ascorbate radical, respectively.

Figures

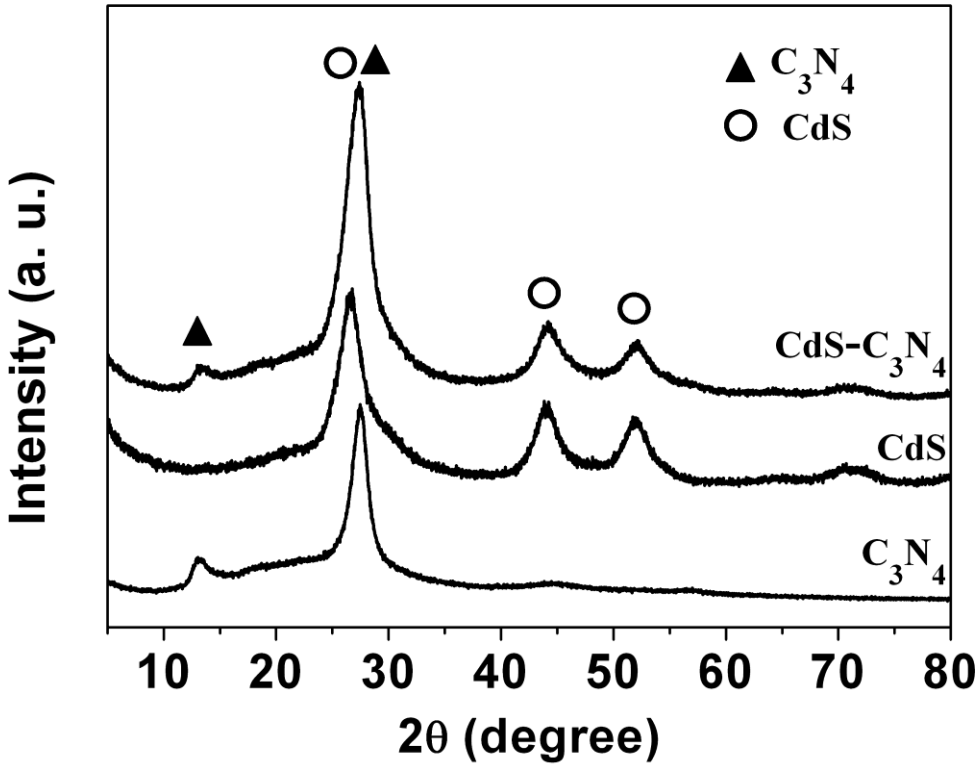

Fig. 1

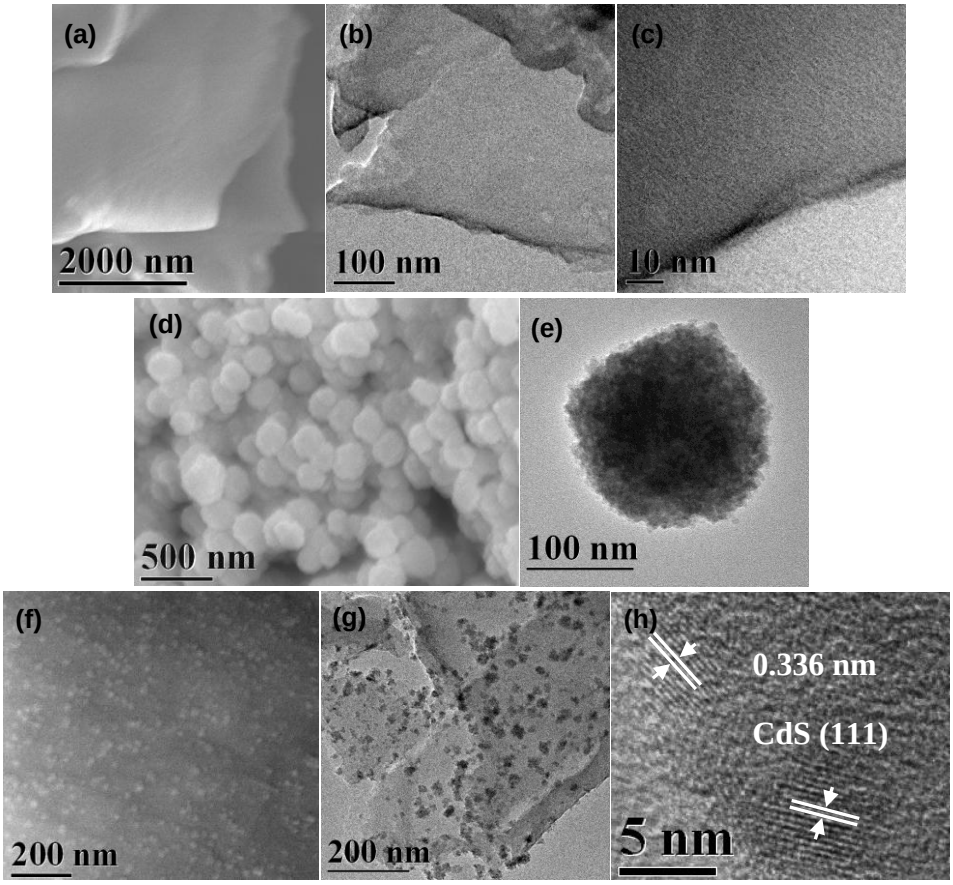
(a)
2000 nm
(b)
100 nm
(c)
10 nm
(d)
500 nm
(e)
100 nm
(f)
200 nm
(g)
200 nm
(h)
0.336 nm
CdS (111)
5 nm

Fig. 2

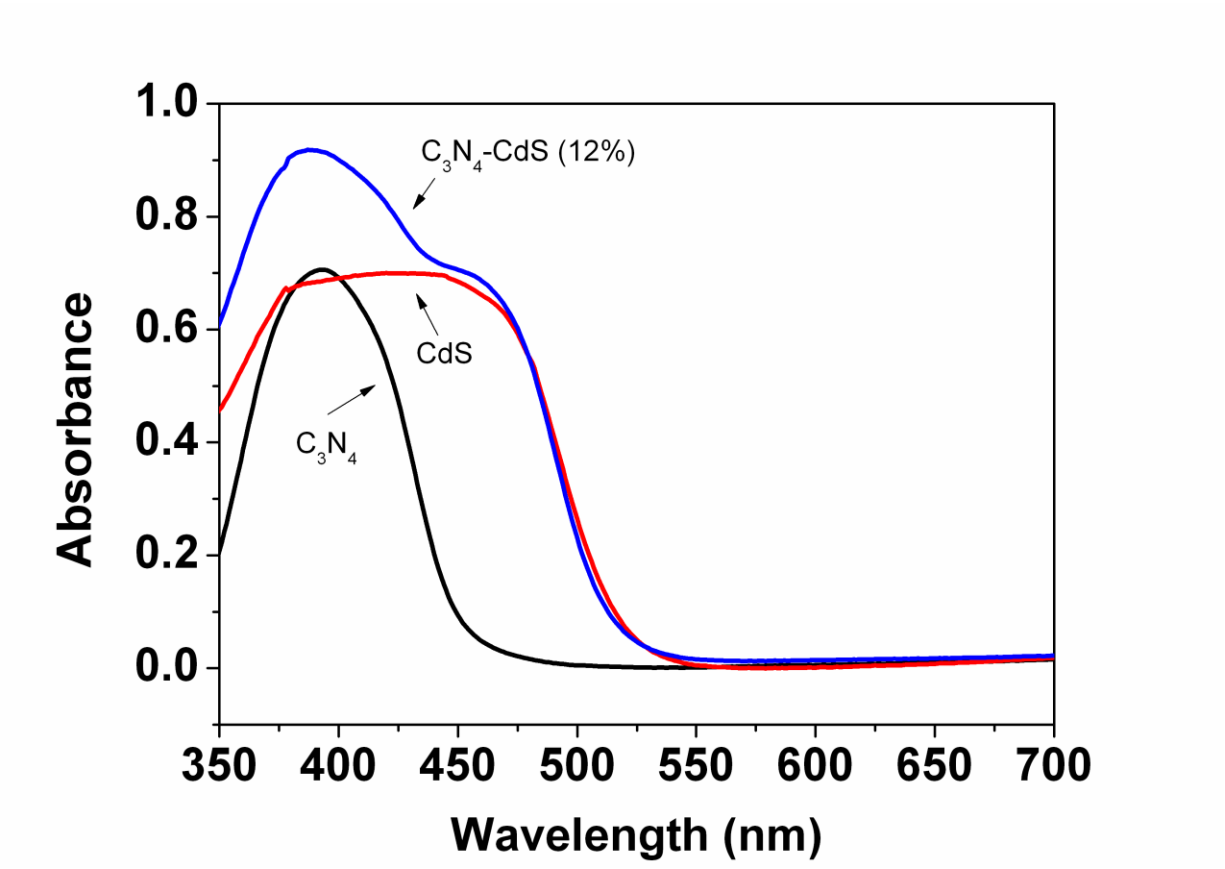
1.0
0.8
0.6
0.4
0.2
0.0
Absorbance
350
400
450
500
550
600
650
700
Wavelength (nm)
C3N4-CdS (12%)
CdS
C3N4

Fig. 3

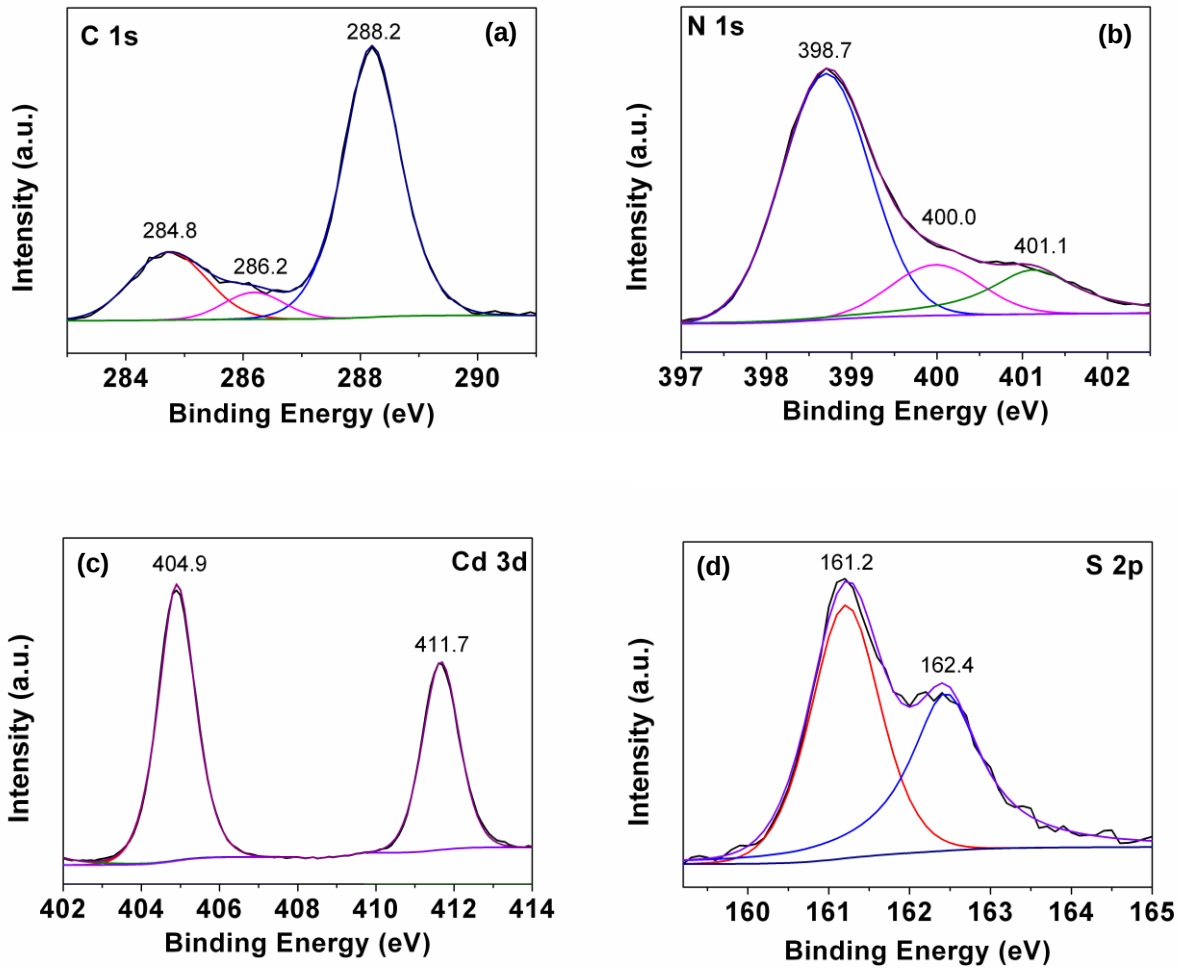
C 1s
(a)
288.2
284.8
286.2
Intensity (a.u.)
284
286
288
290
Binding Energy (eV)
N 1s
(b)
398.7
400.0
401.1
Intensity (a.u.)
397
398
399
400
401
402
Binding Energy (eV)
(c)
404.9
Cd 3d
411.7
Intensity (a.u.)
402
404
406
408
410
412
414
Binding Energy (eV)
(d)
161.2
S 2p
162.4
Intensity (a.u.)
160
161
162
163
164
165
Binding Energy (eV)

Fig. 4

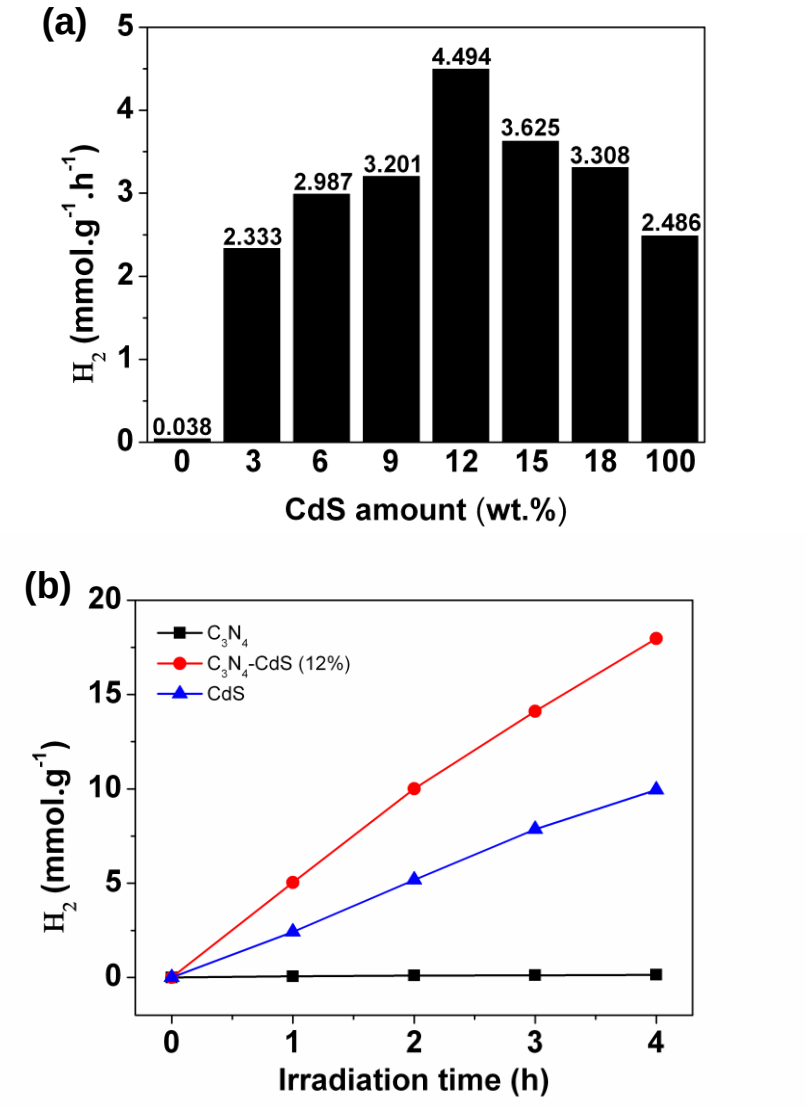
(a)
H2 (mmol.g-1.h-1)
0.038
2.333
2.987
3.201
4.494
3.625
3.308
2.486
0
3
6
9
12
15
18
100
CdS amount (wt.%)
(b)
H2 (mmol.g-1)
C3N4
C3N4-CdS (12%)
CdS
Irradiation time (h)

Fig. 5

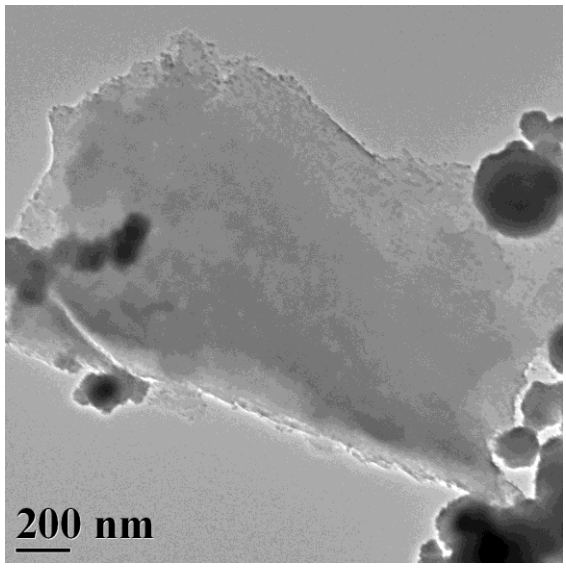

Fig. 6

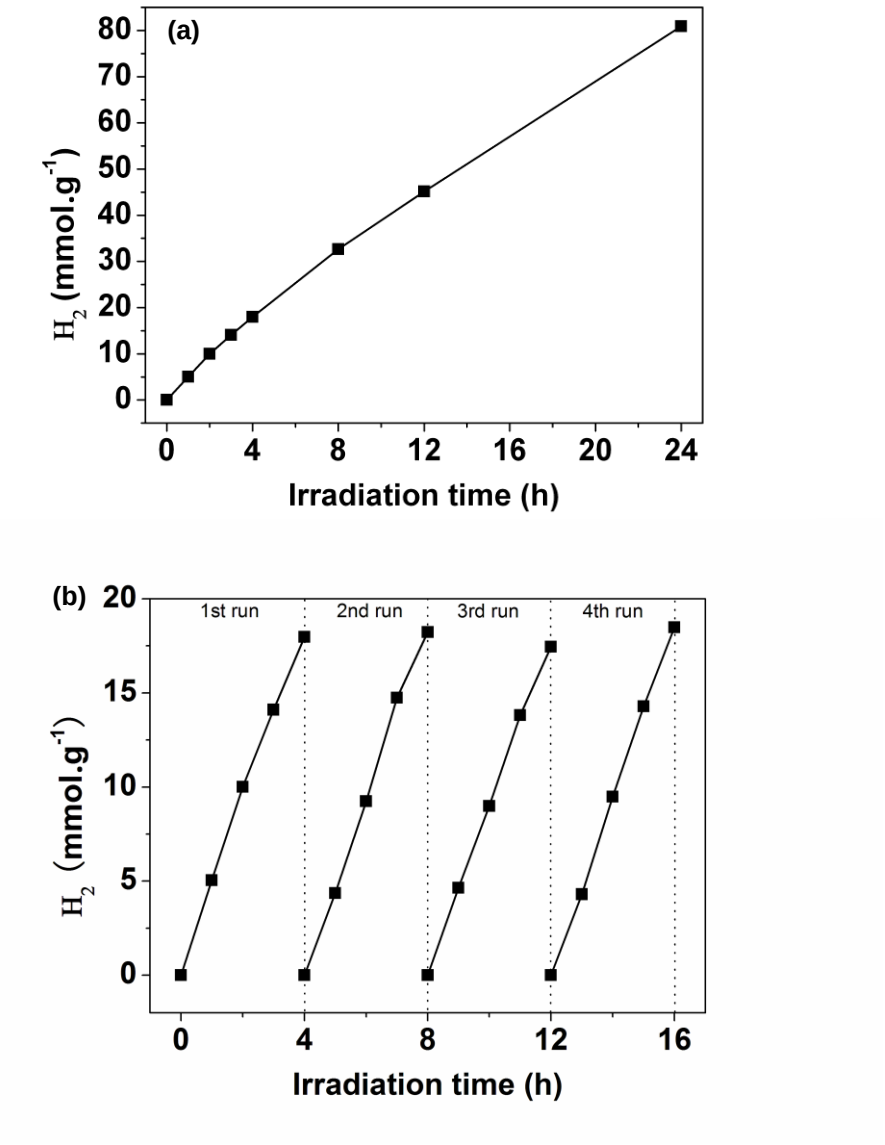
(a)
80
70
60
50
40
30
20
10
0
H_2 (mmol.g^{-1})
0
4
8
12
16
20
24
Irradiation time (h)
(b)
20
15
10
5
0
H_2 (mmol.g^{-1})
1st run
2nd run
3rd run
4th run
0
4
8
12
16
Irradiation time (h)

Fig. 7

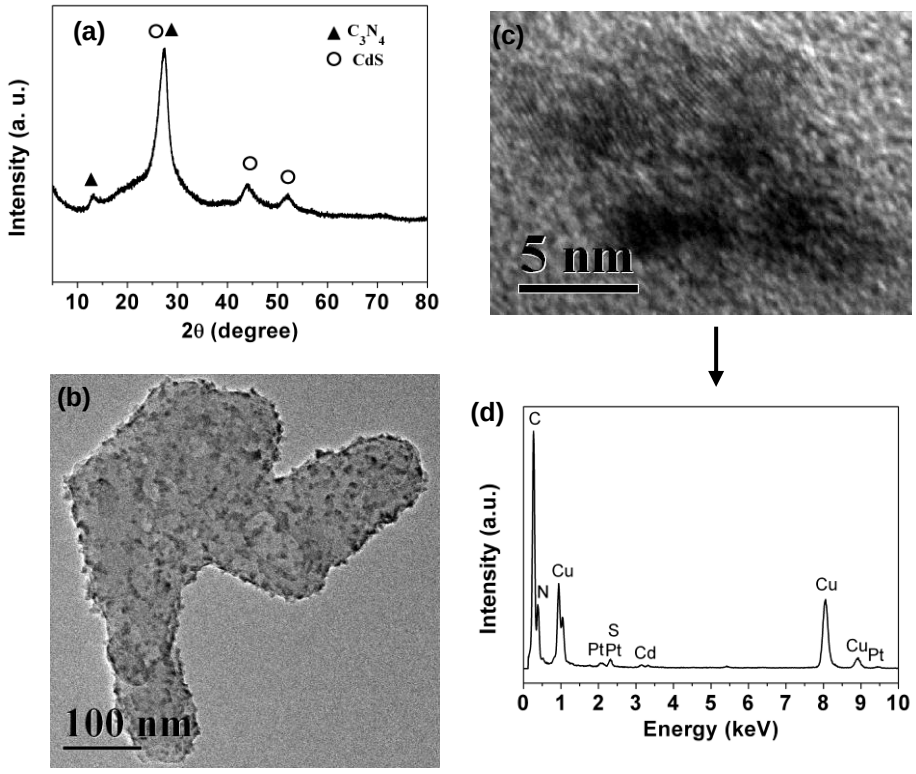
(a)
▲ C_3N_4
○ CdS
Intensity (a. u.)
10 20 30 40 50 60 70 80
2θ (degree)
(b)
100 nm
(c)
5 nm
(d)
C
N
Cu
S
PtPt
Cd
Cu
CuPt
Intensity (a.u.)
0 1 2 3 4 5 6 7 8 9 10
Energy (keV)

Fig. 8

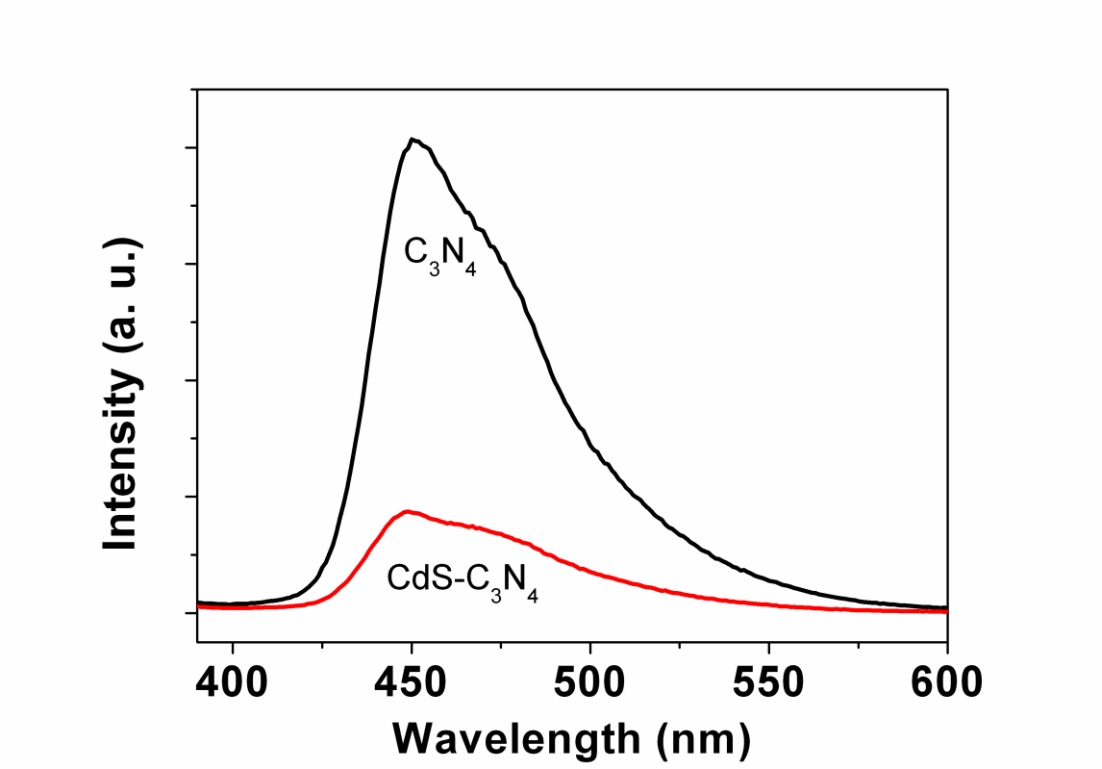

Fig. 9

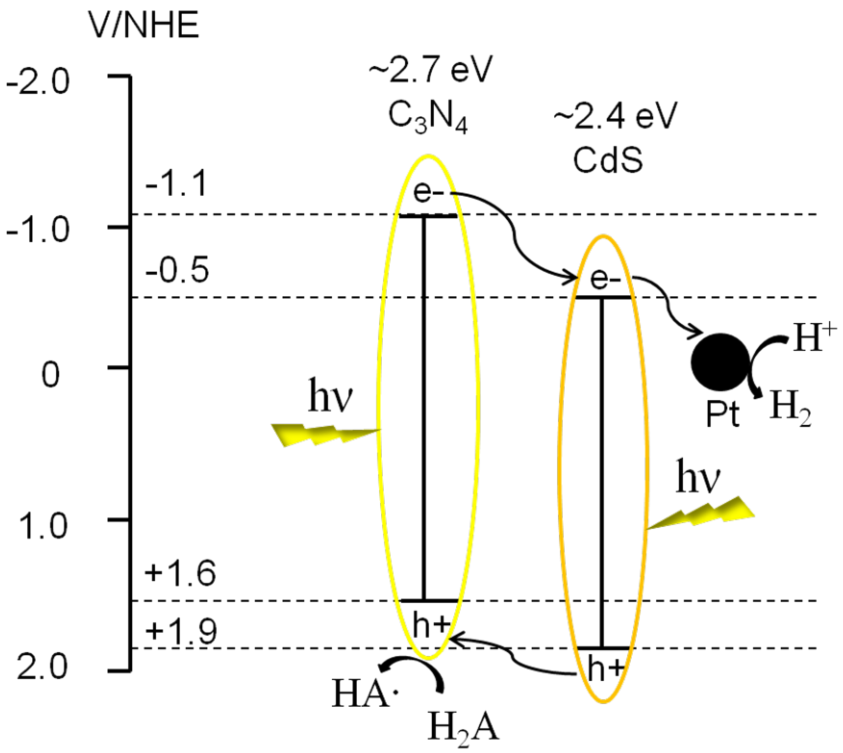
V/NHE
-2.0
-1.0
0
1.0
2.0
-1.1
-0.5
+1.6
+1.9
~2.7 eV
C3N4
~2.4 eV
CdS
e-
e-
hν
hν
h+
h+
H+
Pt
H2
HA·
H2A

Fig. 10